DOI: 10.1002/((please add manuscript number))
Article type: Communication

Differential homeostasis of sessile and pendant epithelium reconstituted in a 3D printed GeminiChip

Pingqiang Cai, Zhuyun Li, Ela Sachyani Keneth, Luying Wang, Changjin Wan, Ying Jiang, Benhui Hu, Yun-Long Wu, Shutao Wang, Chwee Teck Lim, Eugene V. Makeyev, Shlomo Magdassi and Xiaodong Chen**

[*] Prof. X. Chen, Dr. P. Cai, Dr. Z. Li, Dr. C. Wan, Dr. B. Hu, Dr. Y.-L. Wu, Y. Jiang
Innovative Center for Flexible Devices (iFLEX), School of Materials Science and Engineering, Nanyang Technological University, 50 Nanyang Avenue, 639798, Singapore
E-mail: chenxd@ntu.edu.sg
Webpage: http://www.ntu.edu.sg/home/chenxd/

Prof. S. Magdassi, E. S. Keneth
Institute of Chemistry, Centre for Nanoscience and Nanotechnology, The Hebrew University of Jerusalem, Jerusalem 91904, Israel.

Prof. S. Wang, Dr. L. Wang
CAS Key Laboratory of Bio-inspired Materials and Interfacial Science, Technical Institute of Physics and Chemistry, Chinese Academy of Science, Beijing, 100190, P. R. China.

Prof. C. T. Lim
Mechanobiology Institute, Department of Biomedical Engineering, National University of Singapore, 5A Engineering Drive 1, Singapore 117411.

Prof. E. V. Makeyev
Centre for Developmental Neurobiology, King's College London, New Hunt's House, London SE1 1UL, UK.

Keywords: organ-on-a-chip; 3D printing; epithelial homeostasis; mechanobiology; tumor spheroid

Abstract

Local mechanical cues can affect crucial fate decisions of living cells. Transepithelial stress has been discussed in the context of epithelial monolayers, but the lack of appropriate experimental systems led current studies to approximate it simply as an in-plane stress. To evaluate possible contribution of force vectors acting in other directions, we reconstituted double epithelium in a 3D-printed GeminiChip containing a sessile and a pendant channel. Intriguingly, the sessile epithelia were prone to apoptotic cell extrusion upon crowding,

whereas the pendant counterpart favored live cell delamination. Transcriptome analyses showed upregulation of RhoA, BMP2 and hypoxia signaling genes in the pendant epithelium, consistent with the onset of an epithelial-mesenchymal transition program. HepG2 microtumor spheroids also displayed differential spreading patterns in the sessile and pendant configuration. Using multilayered GeminiChip, our results uncover a progressive yet critical role of perpendicular force vectors in collective cell behaviors and point at fundamental importance of these forces in the biology of cancer.

Mechanical forces are known to regulate biological processes such as wound healing, embryogenesis, and growth. Extracellular mechanical cues at the cell-matrix interface can be transduced into intracellular signaling *via* the localization and activation of mechanoresponsive proteins, conformational changes of cytoskeleton architectures and stretch-sensitive ion channels. External and internal mechanical forces cooperatively regulate cellular physiology and tissue-level homeostasis[1-3]. Recently, the importance of a dynamic biomechanical microenvironment in the homeostasis of epithelial monolayers has been highlighted[4]. It is known that the number of epithelial cells in the epithelium is maintained through the extrusion of apoptotic cells[5] and/or delamination of live cells[6]. During this process, intercellular and extracellular matrix (ECM) interactions actively adapt to cell density and local mechanical stresses. Several studies have implied the role of transepithelial stresses in epithelial maturation and functioning[7-12]. In micropatterned epithelium, cells along the rim of the pattern transitioned from two-dimensional (2D) into three-dimensional (3D) structures as a result of geometrical confinement[7]. Furthermore, in contrast to the formation of polarized planar epithelial sheets in conventional 2D cell cultures, 3D cultures can facilitate the autonomous formation of spherical luminal epithelial monolayers, implying that non-planar stresses are involved during lumen formation in 3D cultures[8]. Advancing epithelial monolayers are

reported to regulate their migration by mechanically sensing the thickness of the underlying soft substrate bonded to a stiff support[11]. Moreover, increased hydrostatic stresses perpendicular to the planar monolayer have been shown to compromise the integrity of the epithelium and cause transient cracks to form independently of planar epithelial tension[9]. The mechanical asymmetry of polarized epithelial layers is also revealed by the ability of apical tight junctions to withstand higher transepithelial pressure differences than basal adherens junctions[10]. By taking the accumulative transmural pressure as the morphogenetic driving force, arrays of epithelial domes with arbitrary shapes were formed over non-adhesive areas underlying the planar epithelium[12]. These studies suggest that transepithelial stresses (perpendicular forces through epithelial cells) are important, and new methods to identify their specific contributions to epithelial homeostasis are needed.

Forces experienced by a sessile water droplet are distinct from the pendant droplet[13]. Notably, the perpendicular forces of the droplet-substrate interactions in the pendant droplet are acting against gravitational forces and stretching the droplet, whereas in the sessile configuration, the droplet is perpendicularly compressed. The different equilibrium forces attained in both configurations of the water droplet resemble the perpendicular forces that epithelial cells might experience. It has been shown that intracellular contractility against gravitational forces can regulate the growth of eukaryotic cells by stabilizing cell cytoskeletons and interfering with the sedimentation and fusion of protein droplets[14]. Typically, piconewton forces are potent enough to stimulate conformational changes in force sensor proteins of cells[15]. Therefore, we were inspired to recreate such differential mechanical microenvironments by growing epithelial cells in the sessile and pendant configuration. We hypothesize that epithelial cells grown in the different configuration experience differential mechanical microenvironments that can affect epithelial homeostasis, probably through the progressive effect on the intercellular and cell-matrix interactions.

Microfluidics have been widely used to recapitulate the physiological and pathological microenvironments[16,17]. Here, we fabricated a 3D-printed *GeminiChip* to grow sessile and pendant epithelium and observed that these configurations, which present different mechanical microenvironments, affect the pattern of epithelial homeostasis by altering the mechanical cohesion and genetic expression of epithelial cells. Sessile epithelium, which experienced transepithelial compression, tended to undergo apoptotic cell extrusion whereas, pendant epithelium that were under transepithelial tension favored live-cell delamination upon cell overcrowding. Genetic analyses suggest that transepithelially tensile microenvironments in the pendant epithelium endowed epithelial cells with mesenchymal-like properties. These differences in epithelial homeostasis were also seen in liver tumor models, suggesting that transepithelial stresses are important in the mechanogenetic regulation of epithelial homeostasis, tumor spreading, and likely other patho-/physiological processes.

To recapitulate biologically-relevant transepithelial stresses in a chip, we considered the actin droplet model, which shares similar biophysical properties with lipid droplets and living cells[18]. Actin droplets on glass substrates formed in the sessile and pendant configuration presented different contour profiling (Figure. S1). Compared to the sessile droplet, the pendant droplet showed a higher height but smaller spreading radius. The equilibrium of gravitational forces, droplet-substrate interactions and surface tension were different for the (1) sessile droplet and pendant droplet (2):

$$f_{\perp,Sessile} = g - f_{la} \sin \theta_{Sessile}, \qquad (1)$$

$$f_{\perp,Pendant} = g + f_{la} \sin \theta_{Pendant}, \qquad (2)$$

where $\theta_{Pendant} > \theta_{Sessile}$. Such a perpendicularly compressive press in the sessile droplet and perpendicularly tensile pull on the pendant droplet[13] could contribute to the observed differences in droplet height and radius.

Inspired by the varying mechanical environments experienced by the sessile and

pendant actin droplets, we used 3D printing to create a multilayered microfluidic biochip (known as *GeminiChip*, **Figure 1**a) that allows both sessile and pendant epithelium to exist on one chip. Microfluidics-based biochips are widely used to reconstitute miniaturized tissue analogues and 3D printing is a simple and precise method for creating multilayered channels with lateral accuracy of tens of microns and vertical accuracy of microns[19]. The *GeminiChip* consists of vertically stacked sessile and pendant channels, two independent fluidic channels and, inlet and outlet ports attached on the side walls. The printed chip is transparent for live cell imaging (Figure 1b), and is 40 mm long, 20 mm wide and 1.5 mm thick (Figure S2a). The total chip height including the sessile and pendant channels, and the thickness of the separator and bottom layers is 100 µm. Scanning electron microscopy imaging of the printed *GeminiChip* after laser cutting and introduction of fluids containing red and green dyes into the channels confirmed the multilayered architecture (Figure 1c, d).

Epithelium is formed in two steps (Figure S2b). Madin-Darby canine kidney (MDCK) cells were first seeded in the pendant channel (red) and allowed to form an epithelial monolayer. The chip was then inverted before cells were seeded in the sessile channel (green). Cells in the pendant channel form the pendant epithelium after inversion of the chip while cells in the sessile channel form the sessile epithelium. Cells cultured on the printed materials remained viable after one week (Figure. S3a). Live cell imaging supplied with medium (37°C, infused with 5% CO_2, Figure S3b) showed that the sessile and pendant epithelium (labelled with green and red cell tracker dyes, respectively) were successfully formed (Figure 1e).

Using the *GeminiChip*, we investigated the epithelial homeostasis of the sessile and pendant epithelium monolayers. Upon overcrowding, cells extruded from the sessile epithelium tended to be round and apoptotic-like (**Figure 2**a) as confirmed by caspase staining (green in Figure 2b) and cell counts (Figure 2c). The sessile monolayer was well-maintained, and the contractile ring of actin stress fibers were seen at the site of cell extrusion, which dilated

gradually from the basal plane to the apical plane (Figure 2b, d). The cortex actin of the sessile epithelium appeared to closely encapsulate the nucleus. In contrast, cells delaminated from the pendant epithelium tended to form double- or multi-layered microdomains and remained viable as shown by negative caspase staining (Figure 2a-d). The multi-layered architecture suggests that the integrity of the pendant epithelium was likely disrupted. The cortex actin of pendant epithelial cells appeared to stretch away from the nucleus and the nuclei were oriented more perpendicular rather than parallel to the basal epithelium plane (Figure 2d). Together, these observations show that the homeostasis of sessile and pendant epithelium is different.

The dynamic process of cell extrusion further indicates that the mechanical microenvironments in the sessile and pendant epithelium were regulated differently (Figure 2e). In the sessile epithelium, adjacent cells firstly organized themselves into a tight rosette (Figure 2f). Cooperative contraction of cells in the rosette gradually evicts the target cell out of the monolayer upon triggering the caspase cascade. During the whole process, the apoptotic-cells were well constrained by the rosette-like organization with little lateral displacement. By contrast, the pendant epithelium is characterized by the loss of intercellular tight junctions between the target cells and adjacent cells in the monolayer. The loss of tight junctions loosens the target cells, causing them to migrate and overlap with adjacent cells before escaping from the basal layer without triggering the caspase cascade. The delaminated cell remained viable for hours and could robustly translocate and undergo cell division shortly after delamination (Figure 2e, Figure S4a). Unlike apoptotic-cell extrusion in the sessile epithelium, delaminated cells in the pendant epithelium tended to stay on top of adjacent cells (Figure 2f). In both cases, cell eviction followed a step-by-step process, which might suggest that the epithelial cells have an adaptive and progressive character towards stresses perpendicular to the epithelial monolayers.

Because the nucleus is the largest organelle in the cell and is known to change shape in

response to local mechanical stresses[20], we further examined the effects of epithelium maturation (in terms of cell density) on cell nucleus area and roundness after 3 days of culture (Figure S5). Within the basal monolayer (excluding the delaminated layer), pendant cells packed at approximately 4,900 cells per mm^2 while sessile cells achieved a density of around 7,800 cells per mm^2. Furthermore, pendant epithelial cells exhibited a higher projected nucleus area and nucleus roundness than sessile cells. The less dense basal layer and the larger and rounder nucleus in the pendant epithelium indicate a less crowded microenvironment that is subjected to lower intercellular tension, which likely contributed to the delamination of live cells seen in the pendant epithelium shown in Figure 2.

Following this, the mechanical interactions at the cell-ECM interfaces were further investigated. We used nanomechanical traction stress microscopy[21] to follow the evolution of traction forces in the sessile and pendant epithelium during maturation. To exclude the possible influence of different epithelium geometry (size and shape) on the process, traction stress of micropatterned epithelia (*circle*, diameter of 60 µm) with varying cell density was respectively mapped in the sessile and pendant configuration (**Figure 3**a). Due to limitations in the fabrication of substrates for nanomechanical traction stress microscopy, we conducted the experiments on glass substrates instead of the *GeminiChip*. A similar disparity in epithelial homeostasis was observed between the micropatterned sessile and pendant epithelia (Figure 3b, Figure S4b). The average traction among the sessile epithelia decreased as the cell density increased from low (1-5 cells/patch), to medium (6-10 cells/patch) and high density (> 10 cells/patch). By contrast, average traction stress in pendant epithelia increased from low to medium cell density, followed by a decrease from medium to high density (Figure 3c). Moreover, in comparison to the fading traction stress at the intercellular boundaries of the sessile epithelia in the late stage of maturation, traction stress remained at the intercellular boundaries of the pendant epithelia (Figure 3b). This suggests the loss of mechanical cohesion

in the pendant epithelial cells, which is consistent with the architecture of the multilayered pendant epithelium shown in Figure 2d.

Focal adhesions in the sessile and pendant epithelia (Figure 3d) were also consistent with the pattern of traction stress development in terms of average localizations (Figure 3e) and total area (Figure 3f) of focal adhesions. At high cell densities, focal adhesion protein, paxillin, was seen at the intercellular boundaries of the pendant epithelia, whereas little or no paxillin was observed in the sessile epithelium (Figure 3d). Importantly, the presence of focal adhesions could contribute to traction stress seen along the intercellular boundaries in the pendant epithelia, and implies the loss of epithelial cohesion in them.

Disruption of the epithelial cohesion in the mature and overcrowded pendant epithelium was further confirmed by the disorganized and gradually weakened intercellular adherent junction, E-cadherin (Figure 3g). For the sessile epithelium, the maturation of intercellular cohesion was accompanied by epithelial maturation and a rosette-like organization upon local overcrowding. This maturation was well maintained from the basal plane to the apical plane. Within the identical area, the total length of cell boundaries and total area of regions with fluorescent signal above a threshold in the pendant epithelium was significantly higher (~1.8 fold for total length, ~1.6 fold for total area) than that in the sessile epithelium (Figure S6). This suggests a higher extent of cell overlap and E-cadherin disorganization in the pendant epithelium.

Given the 3D character of the multi-layered domains in the pendant epithelium is clearly different from those seen in the sessile epithelium, we assumed that in addition to in-plane stresses, different transepithelial stresses (mechanical forces perpendicular to the epithelial sheets) are at play in both configurations (Figure 3h). We hypothesized that the sessile epithelium is subjected to transepithelial compression, whereas the pendant epithelium experienced transepithelial tension. To investigate this, we micropatterned larger MDCK

colonies (100 μm diameter circles) onto soft (3 kPa) fibronectin-coated polyacrylamide substrates (~ 70 μm thick) containing a monolayer of fluorescent nanobeads beneath the surface (Figure S7). With a soft substrate, transepithelial stresses experienced by the cells could be inferred from the perpendicular deformation of the substrate. In the sessile epithelium, the underlying substrate was pushed inward towards the nanobeads, implying that the sessile epithelium was undergoing transepithelially compressive stresses (Figure 3h), which is consistent with previous reports[22]. This transepithelial compression might be attributed to the strong intercellular tension, σ_t, and the counter-forces of substrate deformation. In contrast, no significant substrate deformation was observed in the pendant epithelium and cells were more perpendicularly aligned to the substrate, suggesting that pendant epithelial cells were subjected to transepithelial tension likely resulting from σ_g and the attenuating σ_t.

We next examined the gene expression of the sessile and pendant epithelial cells using RNA sequencing (RNA-seq) and reverse transcription-quantitative PCR (RT-PCR). The transcriptomes for both epithelia were different (see **Figure 4**a, Figure S8a for RNA-seq analyses and Figure S8b for RT-qPCR). Notably, several genes known to overexpress in tumor tissues were upregulated in the pendant epithelium, such as LOX, CDH3, TGB2, SNAI2, BLC2A1, VEGFA, *etc*. Meanwhile, genes known to be deregulated in tumor tissues were also downregulated in the pendant epithelium, including CADM1 and NOTCH3 (Figure 4a, left panel). The protein encoded by BCL2A1 gene is known to reduce the release of pro-apoptotic cytochrome c and block caspase activation[23]. The upregulation of BCL2A1 gene (2.27 fold) in the pendant epithelial cells may contribute to decreased caspase activation and apoptosis. Similarly, NOTCH3, a tumor suppressor that induces cellular senescence[24], was also downregulated to 0.41-fold in the pendant epithelial cells. The SNAI2 gene encoding a Snail-family factor known to repress E-cadherin transcription and dampen their cellular protein levels[25] was upregulated (2.42 fold) in the pendant epithelial cells. SNAI2, which is known to

correlate with the loss of apicobasal polarity of epithelial cells[26], could promote the delamination of epithelial cells. Consistent with the up-regulation of SNAI2, E-cadherin expression was noticeably reduced in the pendant epithelium compared to the sessile group (Figure 3g). CADAM1 has been shown to specifically suppress metastasis without affecting primary tumor growth[27]. The downregulation of CADAM1 (0.46 fold) in the pendant epithelial cells may therefore, contribute to the cells' metastasis-like and motile behaviors.

Moreover, many up-regulated genes in the pendant epithelium were associated with the RhoA-controlled pathway (Figure 4a, middle panel), which is known to promote cell motility and contractility[28]. In addition, the functional annotation of regulated genes in the pendant epithelium uncovered statistically significant up-regulation of genes known to be stimulated by bone morphogenetic protein (BMP, Figure 4a, right panel) (SERPINE1, ORC6, FOSL1, DTL, IRFD1, *etc.*) and down-regulation of genes repressed by BMP (RNASE4, WFDC2, DTX4, PDZK1P1, *etc.*). This suggested that the entire BMP pathway, which is a well-known regulator of epithelial-mesenchymal transition (EMT), might have been activated[29]. The upregulation of BMPs and their receptors are important hallmarks of cancer progression. Importantly, the role of BMP2 in boosting the motility and invasiveness of epithelial cells[30] was consistent with the subsequent translocation of the delaminated cells in the pendant epithelium (Figure 3e). Significantly increased expression of hypoxia-associated genes was also detected in the pendant epithelium (Figure S8). Hypoxia is likely due to poor gas exchange across the multi-layered microdomain in the pendant epithelium, consistent with reports that have shown the stimulation of EMT in fibrotic or tumor microenvironments[31]. The different regulation of these genes was also validated using RT-PCR (Figure S8).

In short, differential patterns of homeostasis emerged in sessile and pendant epithelium (Figure 4b), as a result of transepithelial compression and tension respectively. Overcrowded sessile epithelium experienced elevated intercellular tension and presented a preference for

apoptotic-like cell extrusion, which occurred via the formation of rosette patterns and contraction of purse strings. During cell extrusion, epithelial cohesion and the monolayer structure of the sessile epithelium were well-maintained. In contrast, intercellular junctions in the pendant epithelium were disrupted, allowing cells to overlap with and crawl onto adjacent cells before undergoing live-cell delamination. The emerging dichotomy in homeostasis appeared related to differential gene expression. The upregulation of RhoA, BMP2 and hypoxia signaling pathway in the pendant epithelium could contribute to the impaired intercellular cohesion, disrupted epithelial integrity, and increased cell motility.

Cellular spheroids are regarded as ideal models that approximate living tissues and microtumors, the lamination of which behaves like a "living droplet" and is dominated by the relative strength of intercellular cohesion and cell-ECM adhesion[32]. To further examine the possible effects of transepithelial stresses on living tissues, we investigated the lamination process of microtumor spheroids (liver tumor HepG2) in the sessile and pendant configuration, which would be subjected to compression and tension perpendicular to the adhesive substrates, respectively (**Figure 5**a). The sessile microtumor spheroids laminated with the obvious formation of precursor HepG2 monolayer film and the HepG2 cells maintained an epithelial-like morphology. By contrast, the pendant microtumor spheroids were generally resistant to lamination (Figure 5b, Figure S9a). Single cells were seen to escape from the aggregate, implying the weakening or loss of intercellular cohesion, which likely contributed to the failure of precursor film formation. Particle image velocimetry (PIV) analysis (Figure 5c,d) quantitatively confirmed that the sessile microtumor spheroids underwent robust lamination, as shown by the persistent outward flow of the tumor cells at a relatively high speed (up to 15 μm/h). In contrast, cells in the pendant microtumor spheroids were seen to migrate inward and were less motile, implying that the pendant spheroids likely experienced perpendicular stretch. Similar migration patterns and speeds were also seen with smaller MDCK spheroids in the

sessile and pendant configuration (see Figure S9b-e). While sessile MDCK spheroids showed a robust lamination with the formation of broad lamellipodium, little to no lamination and retracted filopodia were seen with pendant spheroids. Taken together, our results show that transepithelial (perpendicular) stresses can exert a significant influence on tissue-level physiology such as epithelial homeostasis and cancer spreading.

Our study shows that epithelial cells grown in a sessile and pendant configuration within a 3D-printed *GeminiChip* display different epithelial homeostasis. Upon crowding, sessile epithelium displayed a preference for apoptotic-like cell extrusion, where cells formed rosette patterns and contracting purse strings after the caspase cascade without disrupting the epithelial monolayer structure or cohesion. In the pendant epithelium, intercellular junctions were disrupted, allowing cells to overlap with and crawl onto adjacent cells before undergoing live-cell delamination. The different epithelium also showed differences in gene expression, including the upregulation of RhoA, BMP2 and hypoxia signaling pathways in the pendant epithelium. Large HepG2 microtumor spheroids and smaller MDCK spheroids in the sessile and pendant configuration also displayed differential spreading patterns and behavior.

Due to the lack of experimental setup to quantify and vary transepithelial stresses through the epithelium, these stresses have been underestimated and many studies have simplified mechanical stresses on the epithelium as in-plane stress[4]. Transepithelial stresses are, in fact, important because they are prevalent in biological tissues (Figure S10). For example, deep folds in the airway epithelium pushing against each other during bronchoconstriction[33] and duct epithelium in mammary glands undergoing lactation give rise to transepithelial compression, while expanding alveolus and mammary glands undergoing suckling exert transepithelial tension[34]. Similar transepithelial stresses are also found in the urothelium in the urinary tract and the folding epithelium during gastrulation[35]. More importantly, tissue cells can exert perpendicular forces against their surrounding substrate[36]

with a magnitude similar to in-plane stresses[37,38]. Similar to our discovery, it was recently shown that lateral contraction was actively involved in the optic-cup morphogenesis[39], though morphogenesis was previously attributed to the imbalance of apical and basal tension.

It is also worth noting that distinct from other studies that exert high magnitudes of mechanical stimuli over short time scales (e.g., seconds[9] or minutes[40]), cells grown in different configurations within the *GeminiChip* experience non-invasive and subtly varying transepithelial forces over a period of a few days. In this work, the dichotomous epithelial homeostasis in the sessile and pendant microenvironments progressively emerged after days of culturing. This time scale is consistent with the mechanical memory behaviors of stem cells during lineage specification and gene expression[41]. Our results suggest that the progressive dichotomy in epithelial homeostasis under varying transepithelial stresses is likely due to the activation of differential mechanogenetic regulation that occurs on the time scale of days.

It is equally noteworthy that the emerging dichotomy may not be directly ascribed to gravitational forces. One single cell is estimated to undergo gravitational forces approximately lower than 10 pN (assuming that one MDCK cell is a cube of 10^3 μm^3 and its density approximates the water as 10^3 kg/m^3). It is seemingly on the order of forces generated by single motor machineries. However, according to the aforementioned time scale, it was through the progressive disruption of cell-matrix and intercellular interactions, as well as the accompanying different transcriptomes, that probably contributed to differential homeostasis in the sessile and pedant epithelium. In addition, the transepithelial stresses comprises not only the perpendicular forces at the cell-matrix interface, but also includes the perpendicular vectors of intra- and inter-cellular contractility. So far, to our knowledge, we are lacking the access to quantifying such transepithelial stresses, which is on urgent demand according to our discovery.

Given *in vivo* tumors interact mechanically with the surrounding ECM and stromal

tissues, our results show that the perpendicular components of the interfacial interactions are likely important in tumor spreading and metastasis, and these stresses should not be underestimated[34]. Our results show that sessile (perpendicularly compressive) microtumors robustly spread on the adhesive surfaces, whilst pendant (perpendicularly tensile) microtumors showed limited outward spreading and was accompanied by inward spheroid deformation. In the future, it is worth revisiting the play of transepithelial (perpendicular) stresses in a variety of tissue-level physiological and pathological processes because a detailed understanding of the role of these stresses may potentially offer new interventions for such diseases as cancers, abnormal embryonic development.

Supporting Information

Supporting Information is available from the Wiley Online Library or from the author.

Acknowledgements

This project is supported by National Research Foundation, Prime Minister's Office, Singapore, under NRF Investigatorship (NRF2016NRF-NRFI001-21) and the Campus for Research Excellence and Technological Enterprise (CREATE) Programme of Nanomaterials for Energy and Water Management. We thank Dr. Ai Lin Chun for helpful critique.

Received: ((will be filled in by the editorial staff))
Revised: ((will be filled in by the editorial staff))
Published online: ((will be filled in by the editorial staff))

References

[1] T. Das, K. Safferling, S. Rausch, N. Grabe, H. Boehm, J. P. Spatz, *Nat. Cell Biol.* **2015**, *17*, 276.
[2] N. I. Petridou, Z. Spiro, C. P. Heisenberg, *Nat. Cell Biol.* **2017**, *19*, 581.
[3] P. Cai, B. Hu, W. R. Leow, X. Wang, X. J. Loh, Y.-L. Wu, X. Chen, *Adv. Mater.* **2018**, *30*, 1800572.
[4] C. Guillot, T. Lecuit, *Science* **2013**, *340*, 1185.

[5] T. B. Saw, A. Doostmohammadi, V. Nier, L. Kocgozlu, S. Thampi, Y. Toyama, P. Marcq, C. T. Lim, J. M. Yeomans, B. Ladoux, *Nature* **2017**, *544*, 212.
[6] E. Marinari, A. Mehonic, S. Curran, J. Gale, T. Duke, B. Baum, *Nature* **2012**, *484*, 542.
[7] M. Deforet, V. Hakim, H. G. Yevick, G. Duclos, P. Silberzan, *Nat. Commun.* **2014**, *5*, 3747.
[8] F. Pampaloni, E. G. Reynaud, E. H. K. Stelzer, *Nat. Rev. Mol. Cell Biol.* **2007**, *8*, 839.
[9] L. Casares, R. Vincent, D. Zalvidea, N. Campillo, D. Navajas, M. Arroyo, X. Trepat, *Nat. Mater.* **2015**, *14*, 343.
[10] E. Moeendarbary, G. Charras, *Nat. Mater.* **2015**, *14*, 268.
[11] P. Cai, M. Layani, W. R. Leow, S. Amini, Z. Liu, D. Qi, B. Hu, Y. L. Wu, A. Miserez, S. Magdassi, X. Chen, *Adv. Mater.* **2016**, *28*, 3102.
[12] E. Latorre, S. Kale, L. Casares, M. Gomez-Gonzalez, M. Uroz, L. Valon, R. V. Nair, E. Garreta, N. Montserrat, A. Del Campo, B. Ladoux, M. Arroyo, X. Trepat, *Nature* **2018**, *563*, 203.
[13] R. Tadmor, P. Bahadur, A. Leh, E. N'Guessan H, R. Jaini, L. Dang, *Phys. Rev. Lett.* **2009**, *103*, 266101.
[14] M. Feric, C. P. Brangwynne, *Nat. Cell Biol.* **2013**, *15*, 1253.
[15] Y. Sawada, M. Tamada, B. J. Dubin-Thaler, O. Cherniavskaya, R. Sakai, S. Tanaka, M. P. Sheetz, *Cell* **2006**, *127*, 1015.
[16] D. Huh, B. D. Matthews, A. Mammoto, M. Montoya-Zavala, H. Y. Hsin, D. E. Ingber, *Science* **2010**, *328*, 1662.
[17] S. G. Uzel, R. J. Platt, V. Subramanian, T. M. Pearl, C. J. Rowlands, V. Chan, L. A. Boyer, P. T. So, R. D. Kamm, *Sci. Adv.* **2016**, *2*, e1501429.
[18] M. P. Murrell, R. Voituriez, J.-F. Joanny, P. Nassoy, C. Sykes, M. L. Gardel, *Nat. Phys.* **2014**, *10*, 163.
[19] N. Bhattacharjee, A. Urrios, S. Kang, A. Folch, *Lab Chip* **2016**, *16*, 1720.
[20] P. M. Davidson, H. Özçelik, V. Hasirci, G. Reiter, K. Anselme, *Adv. Mater.* **2009**, *21*, 3586.
[21] C. Y. Tay, P. Cai, M. I. Setyawati, W. Fang, L. P. Tan, C. H. Hong, X. Chen, D. T. Leong, *Nano. Lett.* **2014**, *14*, 83.
[22] C. G. Tusan, Y. H. Man, H. Zarkoob, D. A. Johnston, O. G. Andriotis, P. J. Thurner, S. Yang, E. A. Sander, E. Gentleman, B. G. Sengers, N. D. Evans, *Biophys. J.* **2018**, *114*, 2743.
[23] R. Haq, S. Yokoyama, E. B. Hawryluk, G. B. Jonsson, D. T. Frederick, K. McHenry, D. Porter, T. N. Tran, K. T. Love, R. Langer, D. G. Anderson, L. A. Garraway, L. M. Duncan, D. L. Morton, D. S. Hoon, J. A. Wargo, J. S. Song, D. E. Fisher, *Proc. Natl. Acad. Sci. USA* **2013**, *110*, 4321.
[24] H. Cui, Y. Kong, M. Xu, H. Zhang, *Cancer Res.* **2013**, *73*, 3451.
[25] J. P. Thiery, H. Acloque, R. Y. Huang, M. A. Nieto, *Cell* **2009**, *139*, 871.
[26] E. L. Whiteman, C. J. Liu, E. R. Fearon, B. Margolis, *Oncogene* **2008**, *27*, 3875.
[27] F. Faraji, Y. Pang, R. C. Walker, R. Nieves Borges, L. Yang, K. W. Hunter, *PLoS Genet.* **2012**, *8*, e1002926.
[28] S. Huang, D. E. Ingber, *Cancer Cell* **2005**, *8*, 175.
[29] L. J. Ma, M. F. Lu, R. J. Schwartz, J. F. Martin, *Development* **2005**, *132*, 5601.
[30] M. H. Kang, J. S. Kim, J. E. Seo, S. C. Oh, Y. A. Yoo, *Exp. Cell Res.* **2010**, *316*, 24.
[31] P. DelNero, M. Lane, S. S. Verbridge, B. Kwee, P. Kermani, B. Hempstead, A. Stroock, C. Fischbach, *Biomaterials* **2015**, *55*, 110.
[32] G. Beaune, T. V. Stirbat, N. Khalifat, O. Cochet-Escartin, S. Garcia, V. V. Gurchenkov, M. P. Murrell, S. Dufour, D. Cuvelier, F. Brochard-Wyart, *Proc. Natl. Acad. Sci. USA* **2014**, *111*, 8055.

[33] J. A. Park, J. J. Fredberg, *Ann. Am. Thorac. Soc.* **2016**, *13*, S64.
[34] D. T. Butcher, T. Alliston, V. M. Weaver, *Nat. Rev. Cancer* **2009**, *9*, 108.
[35] B. He, K. Doubrovinski, O. Polyakov, E. Wieschaus, *Nature* **2014**, *508*, 392.
[36] N. Gjorevski, C. M. Nelson, *Biophys. J.* **2012**, *103*, 152.
[37] H. Delanoe-Ayari, J. P. Rieu, M. Sano, *Phys. Rev. Lett.* **2010**, *105*, 248103.
[38] S. A. Maskarinec, C. Franck, D. A. Tirrell, G. Ravichandran, *Proc. Natl. Acad. Sci. USA* **2009**, *106*, 22108.
[39] S. Okuda, N. Takata, Y. Hasegawa, M. Kawada, Y. Inoue, T. Adachi, Y. Sasai, M. Eiraku, *Sci. Adv.* **2018**, *4*, eaau1354.
[40] O. Chaudhuri, L. Gu, D. Klumpers, M. Darnell, S. A. Bencherif, J. C. Weaver, N. Huebsch, H.-p. Lee, E. Lippens, G. N. Duda, D. J. Mooney, *Nat. Mater.* **2015**, *15*, 326.
[41] C. Yang, M. W. Tibbitt, L. Basta, K. S. Anseth, *Nat. Mater.* **2014**, *13*, 645.

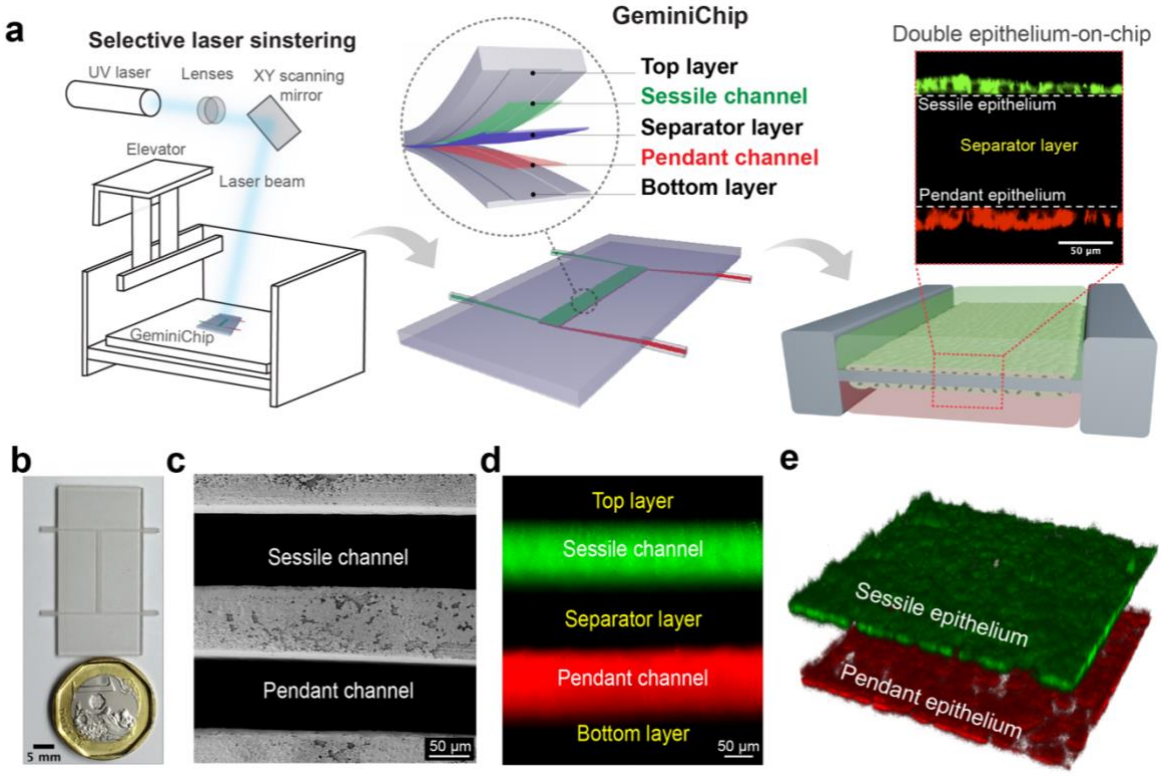

Figure 1. Recapitulation of biologically-relevant mechanical microenvironments in a *GeminiChip*. a) Schematic of the multi-layered *GeminiChip* with epithelium reconstituted in the sessile channel (*green*) and pendant channel (*red*). b) Photograph of the 3D printed *GeminiChip* (left). c) SEM cross-sectional view of the multi-layered structure confirm the presence of the top layer, separator layer and bottom layer. d) Presence of both channels was verified by confocal imaging of fluids containing green and red dyes within the channels (*right*). e) Confocal laser scanning images (left) of reconstituted sessile (labelled with green cell tracker) and pendant epithelium (labelled with red cell tracker) in the sessile and pendant channel, respectively. The 3D reconstruction shows the formation of confluent epithelial monolayers.

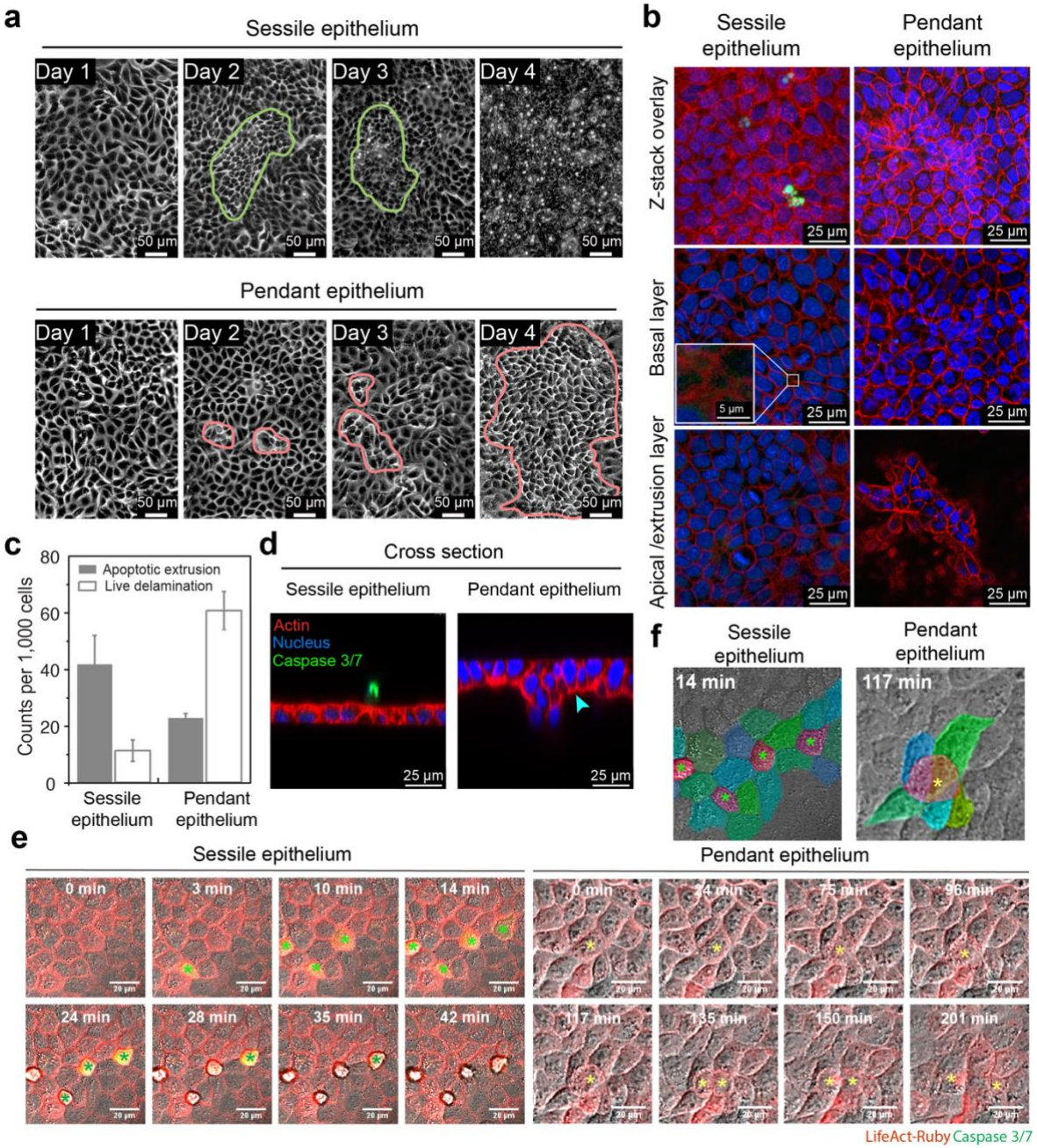

Figure 2. Differential epithelial homeostasis in sessile and pendant epithelium. a) Phase contrast images show epithelial homeostasis is different between overcrowded sessile and pendant epithelium. Green outline shows the region of cell crowding (day 2) and region of extrusion of apoptotic-like cells (day 3), while pink outline shows the region of cell delamination and overlapping. Apoptotic-like cells were also found in the pendant epithelium, but at a lower ratio. Representative images of five different experiments. b) Detection of apoptotic extrusion and live cell delamination in the sessile and pendant epithelium by live caspase probe and confocal laser scanning microscope. *Inset* shows the rosette pattern of cortex actin at the site of apoptotic extrusion. c) Relative ratio of cells undergoing apoptotic extrusion and live delamination. About 40 cells out of 1,000 cells in the sessile epithelium showed apoptotic extrusion, while around 60 cells underwent live delamination in the pendant

epithelium. Data are from three experiments and presented as mean ± s.d. d) Confocal laser scanning imaging shows a localized multi-layered domain in the pendant epithelium, in contrast to apoptotic extrusion from the well-maintained monolayer of the sessile epithelium. *Cyan arrow* shows the detachment of cortex actin from the cell nucleus. e) Live DIC imaging shows the typical process of apoptotic cell extrusion (green asterisk) and live cell delamination (yellow asterisk) in the sessile and pendant epithelium, respectively. Caspase cascade is indicated by CellEvent Caspase 3/7 Green and live cell is visualized with actin marker, LifeAct-Ruby. No caspase cascade is seen during cell delamination in the pendant epithelium. f) Color-coded cells show the live delamination and overlapping of cells in the pendant epithelium, in contrast to the intact epithelial integrity in the sessile epithelium. *Green asterisk*, apoptotic cells undergoing caspase cascade. *Yellow asterisk*, cells escaped by live delamination.

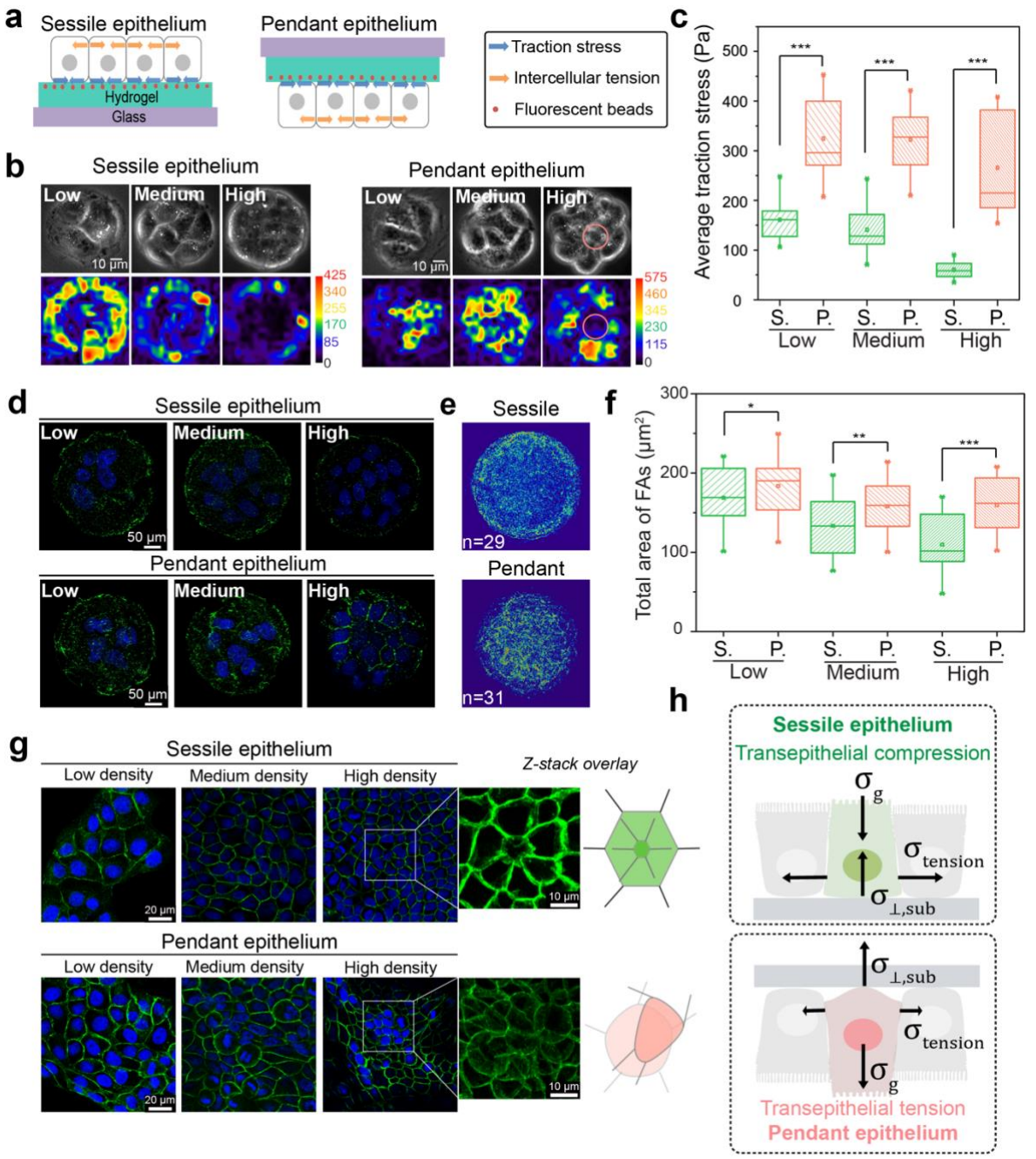

Figure 3. Distinct mechanical evolution in the sessile and pendant epithelium. a) Schematic illustration of sessile and pendant configuration for nanomechanical traction stress microscopy. Epithelial cells were grown on glass substrates coated with polyacrylamide gel (10 kPa) embedded with fluorescent microbeads. b) Phase contrast (top row) and nanomechanical traction stress maps (bottom row) of micropatterned sessile and pendant epithelium at low (1-5 cells/patch), medium (6-10 cells/patch) and high (> 10 cells/patch) cell densities. Representative of >8 samples. Attenuating traction stress in the sessile epithelium suggests a transition from cell-ECM interaction to cell-cell interaction. Such a transition was not observed in the pendant epithelium, rather traction stress emerged at inter-cellular boundaries. *Pink circle* denotes a delaminated cell. c) Box plot shows the average epithelial traction stress changes

with cell density. Traction stress in the pendant (P) epithelium was statistically higher than that in the sessile (S) epithelium. Low, medium and high density correspond to panel (b). d) Representative confocal laser scanning images of focal adhesions (paxillins, green). Nuclei is stained with Hoechst 33342 (blue). e) Averaged color-encoded localization of paxillins in the sessile and pendant micropatterned epithelium. 29 sessile patches and 31 pendant patches were analyzed. f) Box plot showing total area of focal adhesions (FAs) in the sessile and pendant epithelium. Pendant epithelium had a higher expression of FAs and a greater number of FAs along the intercellular boundaries than sessile epithelium. g) Confocal laser scanning images showing the organization of adherent junctions, E-cadherin (green), in the sessile and pendant epithelium upon overcrowding. E-cadherin in the sessile epithelium is well-organized from the basal layer to the apical layer, whereas overlapping occurred in the pendant epithelium, as depicted in the right schematic illustration. *White box*: magnified view and Z-stack overlay of region of interest. * $P \leq 0.05$, **$P \leq 0.01$, ***$P \leq 0.001$ (student's t-test). h) Proposed recapitulation of the transepithelially compressive and tensile microenvironments, respectively. σ_g, $\sigma_{\perp,sub}$, σ_t are gravitational stress, the perpendicular component of the cell-substrate stress and intercellular tension, respectively. All data are shown as mean $\pm$ s.d.

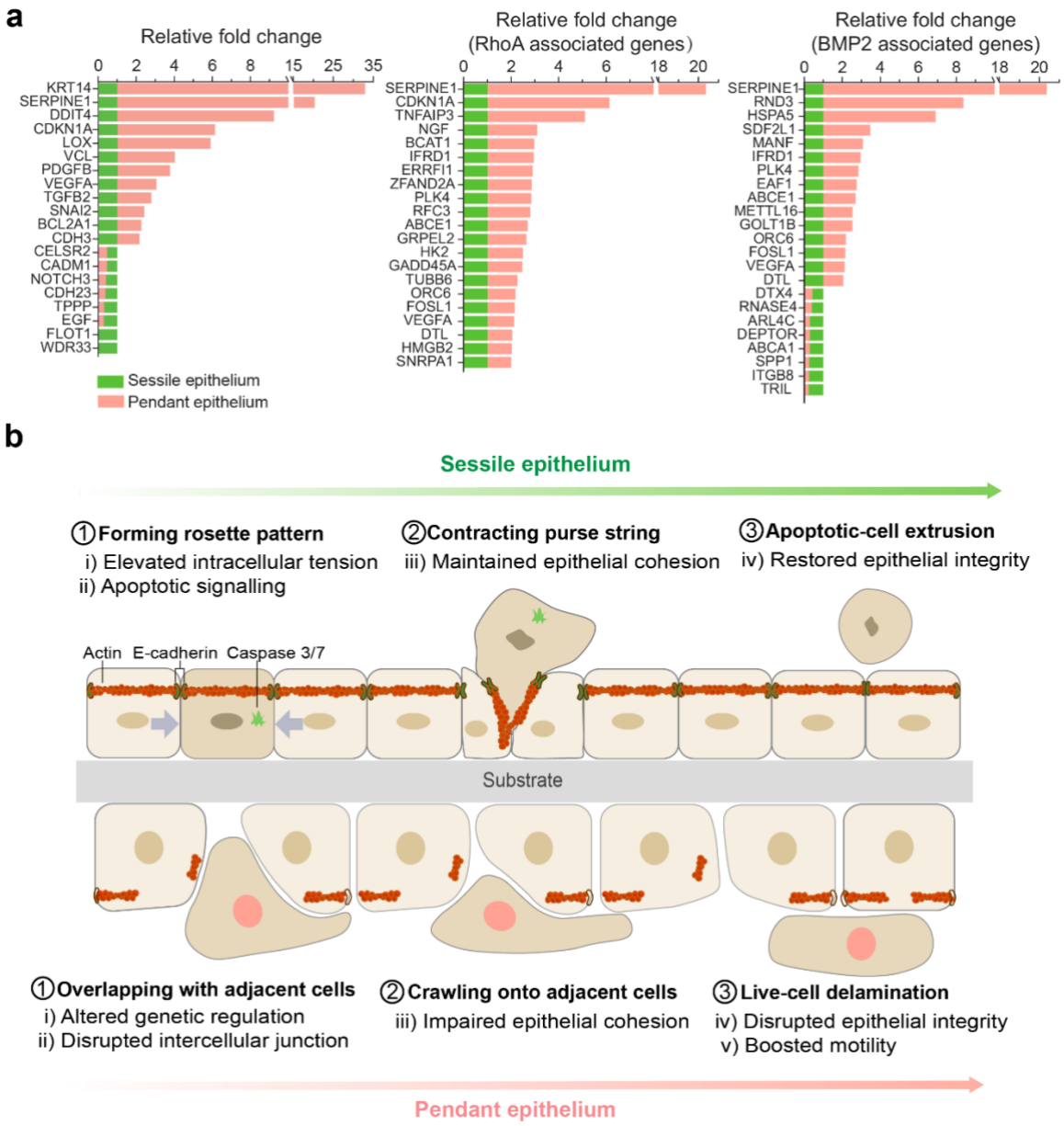

Figure 4. Mechanogenetic coupling and regulation of epithelial homeostasis. a) Bar charts showing relative fold changes in RNA expression of overcrowded pendant epithelium (pink bars) and sessile epithelium (green bars) after 4 days of culture, q-value < 10^{-8}. Left chart shows representative genes typically dysregulated in tumor tissues, including the upregulation of LOX, TGFB2, SNAL2, BCL2A1, CDH3, and the downregulation of CADM1 and NOTCH3. Middle chart shows the expression of RhoA-associated genes , which are known to regulate cytoskeleton reorganization, focal adhesion formation and promote cell motility; upregulation of RhoA genes suggest an increase in cellular motility and/or invasiveness. Right chart shows genes related to the activation of BMP2 pathway, including the upregulation of BMP2 promoters and downregulation of BMP2 suppressors. b) Proposed fate decision of epithelial cells upon overcrowding in the sessile (transepithelially compressive) and pendant (transepithelially tensile) epithelium. Sessile epithelium maintains homeostasis through

apoptotic extrusion, where cells form rosette patterns around the target cell before intercellular tension is increased and purse strings are contracted. In contrast, the altered mechanogenetic regulation in the pendant epithelium leads to disrupted intercellular junctions, enabling the target cell to overlap with and crawl onto adjacent cells before undergoing live delamination.

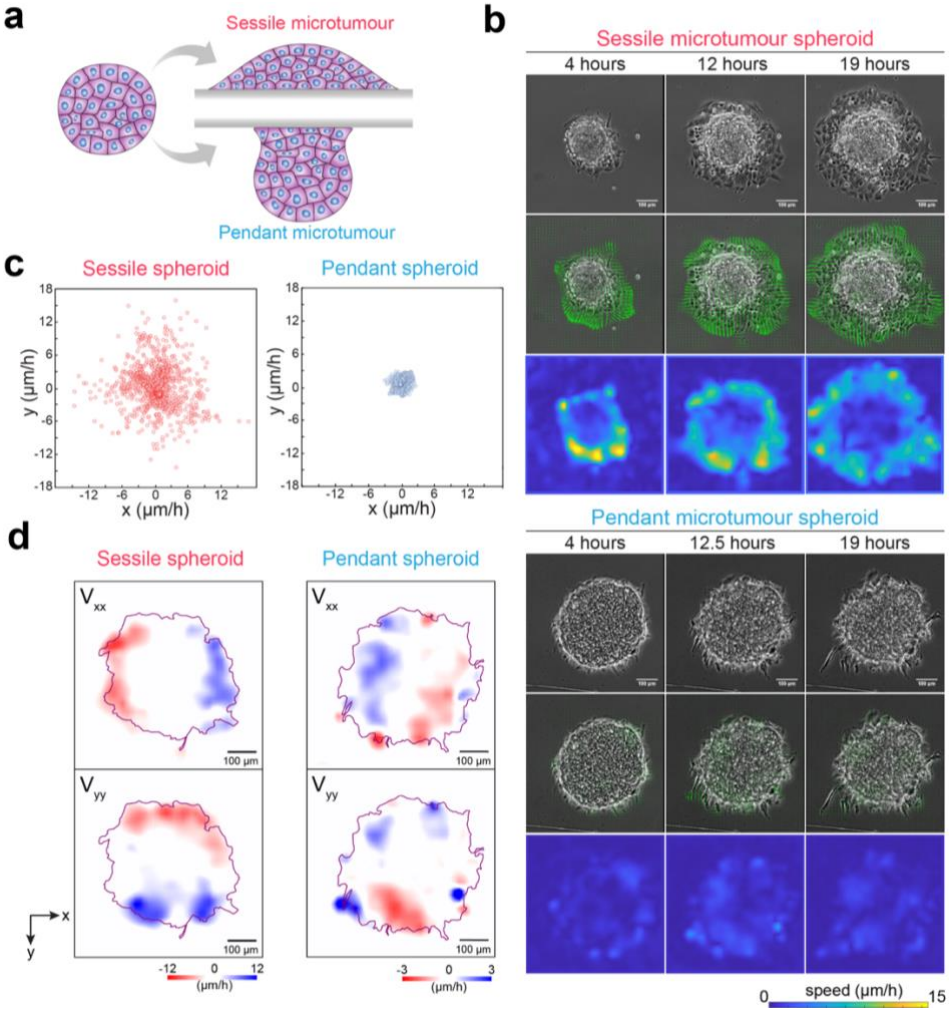

Figure 5. Lamination of liver microtumor models subjected to different perpendicular stresses. a) Scheme showing the sessile (compressive) and pendant (tensile) liver microtumor models (HepG2 spheroids) undergoing lamination. b) Phase contrast (top row), velocity mapping by PIV analysis (middle row) and color-encoded speed magnitude mapping (bottom row) images show the lamination of sessile spheroids is robust with outward flow of tumor cells and formation of lamellipodium, whereas little to no lamination is seen with pendant spheroids. Images are representative of six different spheroids. c) Velocity scatter plot of spreading sessile microtumor (*left, red*) and non-spreading pendant microtumor (*right, blue*), upon 12 hours of lamination. Velocity of the sessile microtumors was significantly higher in both *x* and *y* direction. d) Mapping of the V_{ex} (x component of velocity) and V_I (y component of velocity) in the sessile and pendant microtumor spheroid (12 hours of lamination). Periphery of microtumor spheroids are outlined in purple. Outward spreading in the sessile spheroid is shown in the bi-polarized blue (positive V_{ex} and V_I) and red (negative V_{ex} and V_I), whereas inward deformation flow in the pendant spheroid is shown by the opposite arrangement of the blue and red domains that approximate the spheroid periphery.

Multilayered GeminiChip was 3D printed for reconstituting the sessile and pendant epithelium to disclose the role of cryptic transepithelial stresses in the mechanogenetic regulation of tissue-level homeostasis, which imparts the former with preference towards apoptotic extrusion and the latter towards live delamination, emerging through the dichotomous epithelial tension evolution and genetic expression.

Keywords: organ-on-a-chip, 3D printing, epithelial homeostasis, mechanobiology, tumor spheroid

Pingqiang Cai, Zhuyun Li, Ela Sachyani Keneth, Luying Wang, Changjin Wan, Ying Jiang, Benhui Hu, Yun-Long Wu, Shutao Wang, Chwee Teck Lim, Eugene V. Makeyev, Shlomo Magdassi and Xiaodong Chen**

Differential homeostasis of sessile and pendant epithelium reconstituted in a 3D printed GeminiChip

ToC figure

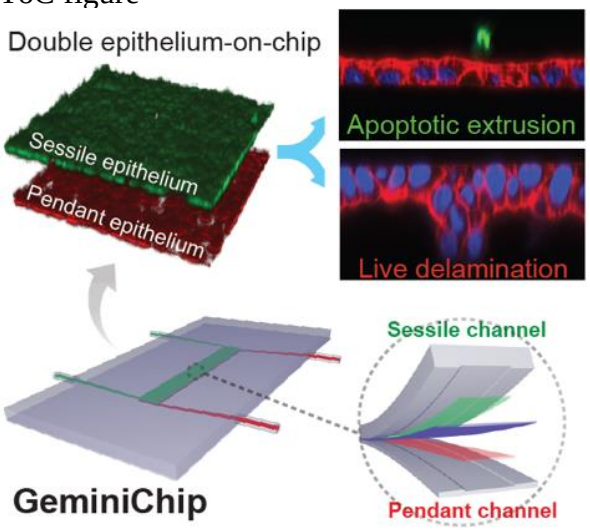

Supporting Information

Differential homeostasis of sessile and pendant epithelium reconstituted in a 3D printed GeminiChip

Pingqiang Cai, Zhuyun Li, Ela Sachyani Keneth, Luying Wang, Changjin Wan, Ying Jiang, Benhui Hu, Yun-Long Wu, Shutao Wang, Chwee Teck Lim, Eugene V. Makeyev, Shlomo Magdassi and Xiaodong Chen**

Experimental Section

3D printing of GeminiChip: The *GeminiChip* was printed using the ink VeroClear-RGD810 (Stratasys, USA) and a soluble support material SUP707 (Stratasys, USA). The whole device was printed in a glossy mode to ensure the transparency of the device, and the removal of the support material was performed by immersing the printed object in deionized water (60 °C) under sonication for 24 hours, followed by a hot water flow through the channels to completely remove remaining support materials.

Immunostaining and apoptosis detection: The sessile and pendant epithelium were rinsed with warm phosphate buffered saline (PBS), fixed with 4% paraformaldehyde and rinsed again with PBS. Membrane permeabilization and blocking were simultaneously conducted with 0.5% Triton X-100 in 10% normal goat serum for 1 hour. Then Alexa 561-conjugated phalloidin (Invitrogen) was used for f-actin staining, and E-cadherin antibody or paxillin antibody was used for E-cadherin staining or paxillin staining respectively. Followed by the subsequent introduction of Alexa 488-conjugated secondary antibody. For live apoptosis detection, 5 μM caspase-3/7 green detection reagent (Invitrogen) was introduced into the channels and incubated for 45 minutes before imaging.

Cell traction stress mapping: Cell traction force microscopy was conducted on polyacrylamide gel films embedded with fluorescent microspheres. To map the traction stress cells exerted on the substrates, the deformation field of the gel substrate was firstly calculated by tracking fluorescent microbeads. The obtained deformation field was then translated into traction stress

according to Green's function. Briefly, the traction force at discrete point $\vec{f_i}$, located at the position (x_i, y_i) was calculated based on the following formula $\vec{u_i}\,(x,y) = \sum_{i=1}^{n} \vec{G}(x - x_i, y - y_i)\,\vec{f_i}$, where $\vec{G}$ denoted the Greens' tensor and $\vec{u_i}$ denoted the experimental displacements of fluorescent beads at position (x_i, y_i). The overall force of the cell $\left|\vec{F}\right|$ is an integral of the traction field magnitude over the area, $\left|\vec{F}\right| = \iint \sqrt{T_x^2(x,y) + T_y^2(x,y)}\,dxdy$, where $T\,(x,y) = [T_x(x,y) + T_x(x,y)]$ is the continuous field of traction vectors defined at any spatial position (x, y) within the cell. Polyacrylamide thin films (elastic modulus: 10 kPa) embedded with a monolayer of fluorescent nanobeads were firstly micropatterned with circle adhesion patches (Fibronectin, ∅ 60 μm) on their surface. Upon adhesion of 1-2 cells onto each patch, the upright and inverted configuration was adopted to form the sessile and pendant epithelia, respectively. Afterwards, cell traction stress mapping was conducted after 1-3 days of culture. In the case of examining transepithelial stresses, polyacrylamide thin films of 3 kPa were used.

Lamination of cellular spheroids: The cellular spheroids formed following the protocol of 3D Petri Dish® (Sigma), using either human cancer cell line HepG2 as microtumor models or MDCK cells. Briefly, sterile molten agarose (2%) filled the autoclaved micro-molds (Z764019-6EA) and gelled at room temperature, followed by cell seeding at the concentration of 1×10^6 cells/mL. Formed cellular spheroids were harvested after 3 days, and seeded onto fibronectin coated coverslips. The sessile spheroid spheroids were allowed to sediment and adhere for 3 hours in the sessile configuration before live imaging of spheroid lamination. The pendant spheroids were allowed to sediment and adhere for 1 hour in the sessile configuration before being inverted into the pendant configuration for another 2 hours, followed by the before the live imaging.

RNA sequencing and RT-qPCR: For RNA sequencing, total RNAs were extracted from the sessile and pendant epithelium using Trizol (Life Technologies). RNA Mini kits (Ambion) were used to prepare 50READS cDNA libraries. RNA sequencing was then conducted by a

MiSeq machine (Illumina). RNA-seq reads were aligned with ENSEMBLE CanFam3.1 genome using TopHat 2.1.0. ENSEMBLE CanFam3.1 gene annotation was updated with MDCK-specific transcripts using StringTie 1.3.0 and gene expression changes were quantified using Kallisto 0.43.0 and Sleuth 0.28.1. For RT-qPCR, total RNA was extracted from the compressive and tensile epithelium using Trizol (Life Technologies) and purified using RNA Mini kits (Ambion). Reverse transcription (RT) was performed in 10 `123µl reactions containing 2.5 µg of total RNA, 50 pmol of a random decamer primer (N10), 40 units of rRNAsin (Promega) and 100 units of SuperScript III reverse transcriptase (Invitrogen) at 50°C for 1 hour. Quantitative PCR (qPCR) assays were run with StepOnePlus real-time PCR system (Applied Biosystems) using SYBR FAST qPCR Master Mix (KAPA Biosystems). The signals were normalized to GAPDH mRNA levels.

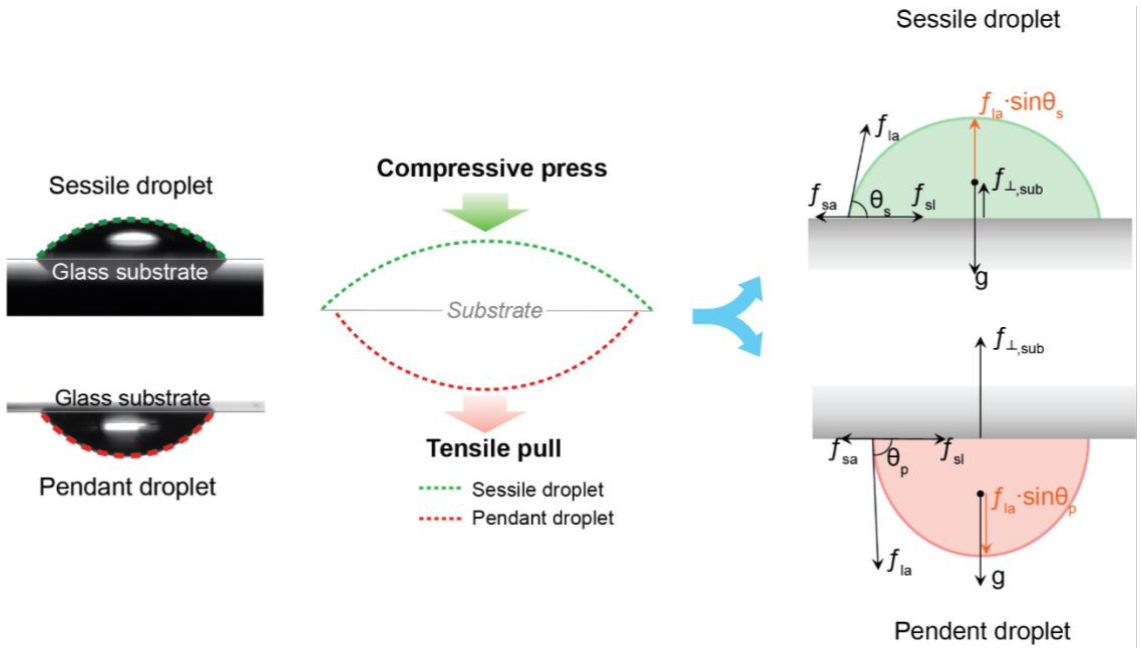

Figure S1. Mechanics of actin droplet model. Optical image (left) and schematic (right) show sessile and pendant actin droplet on glass have different height and spreading radius. Compressive press in the sessile droplet lowers the droplet height and increases its spreading radius. Dashed green and red lines delineate the contour of sessile and pendant droplet, respectively. Data are representative of two 5 µL droplets for both sessile and pendant droplets. Forces acting in the droplet model. Equilibrium of gravitational forces, droplet-substrate interactions and surface tension for the sessile and pendent droplets. Equilibrium force is different for the (1) sessile droplet, $f_{\perp,Sessile} = g - f_{la} \sin\theta_{Sessile}$ and (2) pendant droplet, $f_{\perp,Pendant} = g + f_{la} \sin\theta_{Pendant}$, where $\theta_{Pendant} > \theta_{Sessile}$. Tensile pull in the sessile droplet and compressive press on the pendant droplet cause measurable changes in droplet height and radius on the glass surface. *la, sa, sl* refer to the interface of liquid/air, solid/air and solid/liquid, respectively.

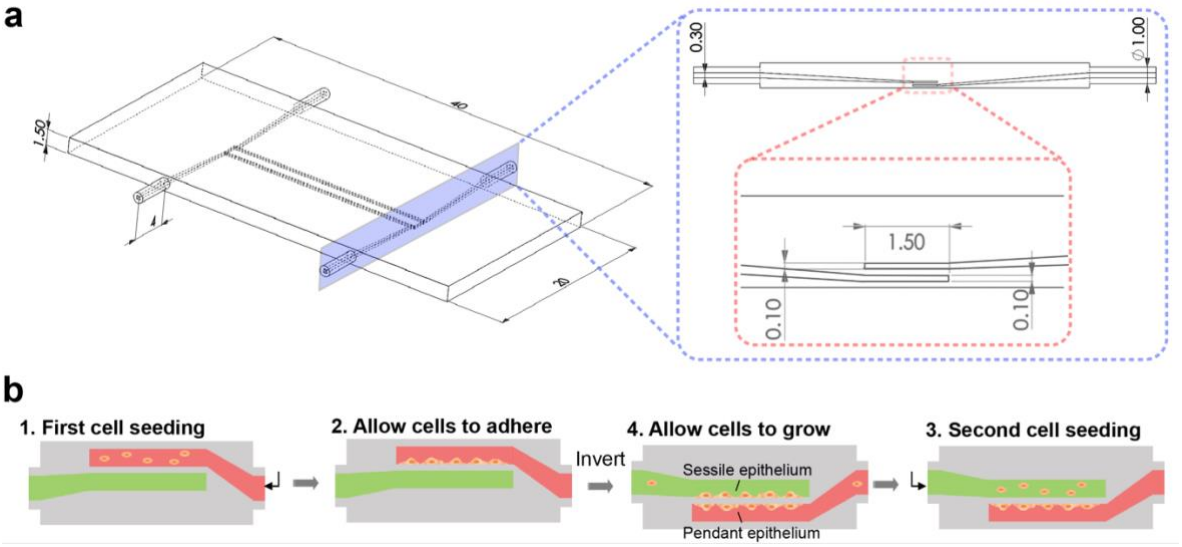

Figure S2. a) Computer-aided-design of the *GeminiChip*. Schematic showing dimensions of the whole device (left) and the cross-sectional view (right) of the violet zone. Red in violet box shows magnified view of the multilayered region. All units are in *mm*. The model was sketched with AutoCAD and exported as .ob. file for 3D printing. b), Procedure for reconstituting sessile and pendant epithelium in *GeminiChip*.

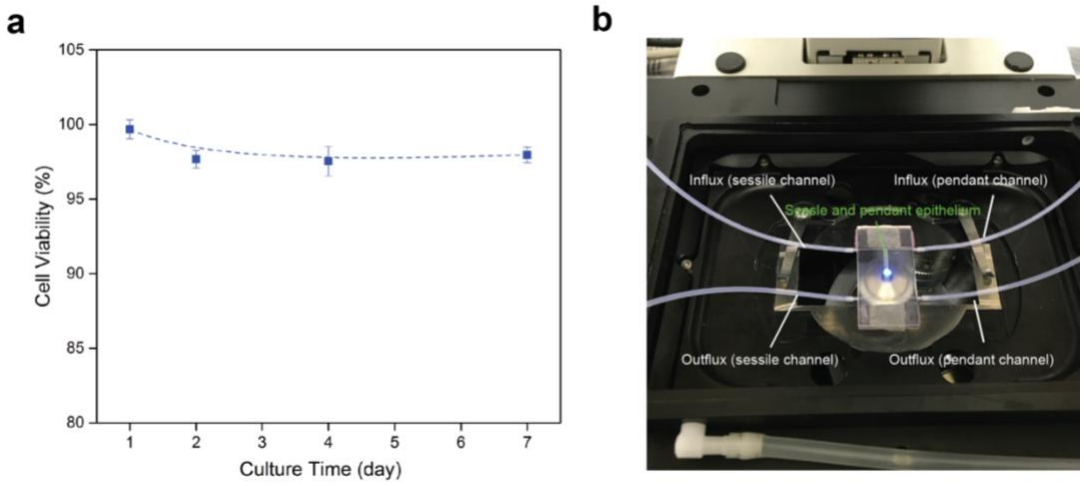

Figure S3. a) Cell viability on printed acrylate film. The printed thin film (thickness: 200 µm) was coated with 25 µg/mL fibronectin before 20 cells/mm^2 MDCK cells were seeded and allowed to grow under 37 ° C with 5 % CO_2 . In the absence of crowding, 98% MDCK cells remained viable after 7 days. Data represent three experiments and are shown as mean ± s.d. b) *GeminiChip* mounted on the confocal laser scanning microscope. The invertible design of the chip allowed the sequential reconstitution of the sessile and pendant epithelium, without the need of disassembling the influx and outflux tubes.

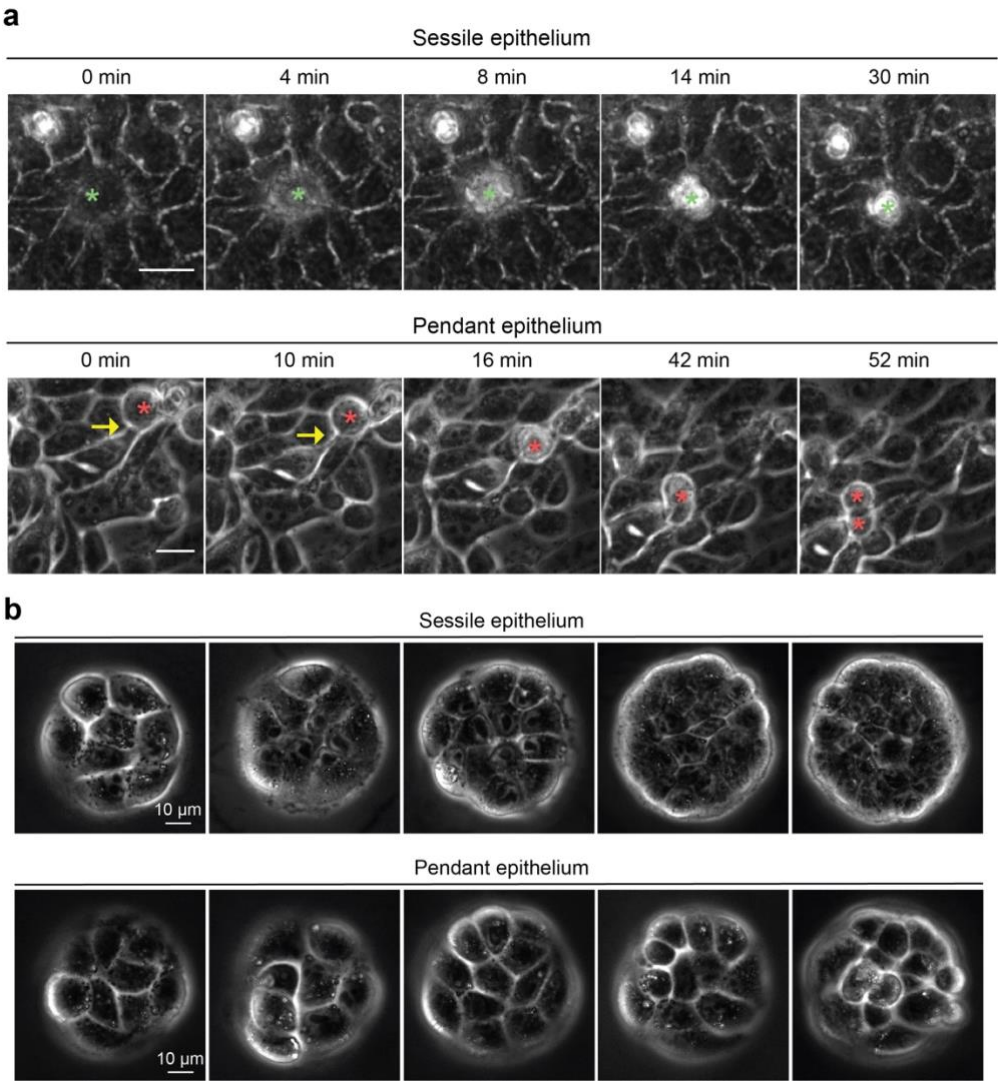

Figure. S4. a) Representative phase contrast images of apoptotic extrusion and live delamination in the sessile epithelium (*upper row*) and pendant epithelium (*lower row*), respectively. *Green asterisk* indicates the cell undergoing apoptotic extrusion with rosette pattern formation of adjacent cells. *Red asterisk* indicates the cell that is undergoing live delamination, followed by robust translocation and subsequent division. *Yellow arrow* shows the gradual loss of inter-cellular contacts. Data are from one experiment representative of three experiments. Scale bar: 20 µm. b) Morphogenesis of micropatterned (*Circle*, diameter of 60 µm.) epithelia in the sessile and pendant microenvironments. Cells were micropatterned on 10 kPa PAA gel. Similar to cells cultured in *GeminiChip*, sessile epithelia showed reliable cohesion and epithelial integrity, whereas pendant epithelia showed disruption. This experiment shows that the different homeostasis observed with sessile and pendant epithelia is not influenced by geometrical confinement of micropatterning.

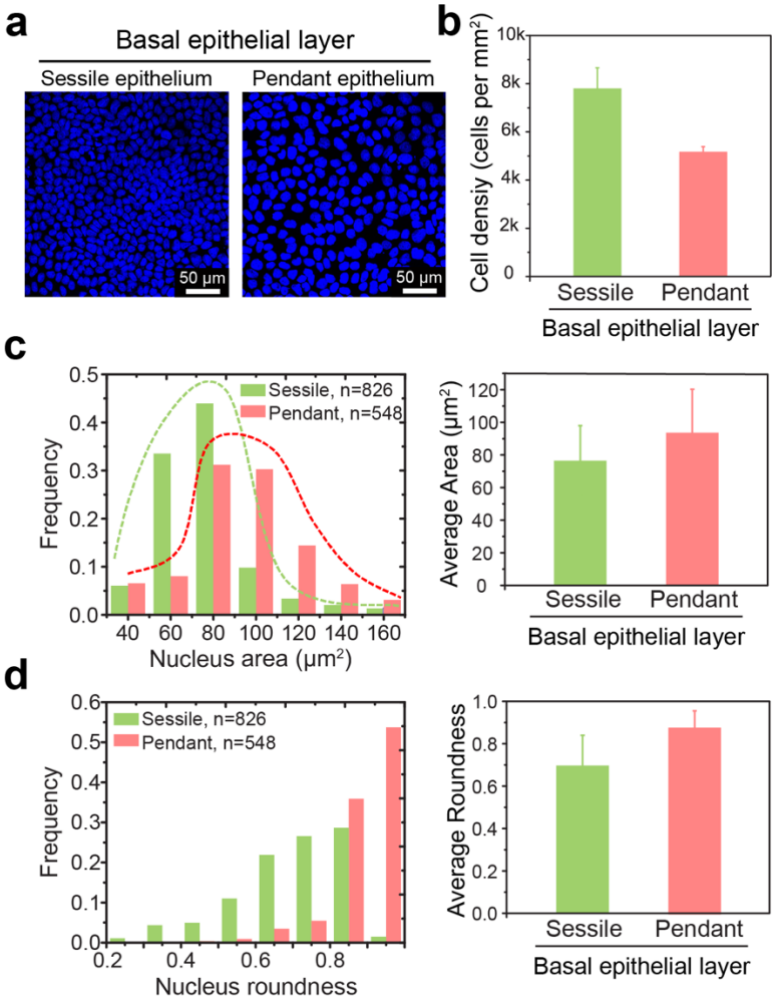

Figure. S5. Confocal laser scanning images a) and the corresponding quantitative data b) showing average cell density in the basal epithelial layer of the sessile and pendant epithelial cells after 3 days of culture. Sessile epithelium was on average denser than pendant epithelium, suggesting higher crowding in the basal epithelial layer of the sessile epithelium. Cell nuclei in the basal layer of the sessile epithelium are larger c) and rounder d) than the pendant epithelium, suggesting that pendant epithelium experiences a lower intercellular tension than sessile epithelium. 826 sessile epithelial cells and 548 pendant epithelial cells (within equal area of interest) were analyzed by Leica Application Suite. Data are shown as mean ± s.d.

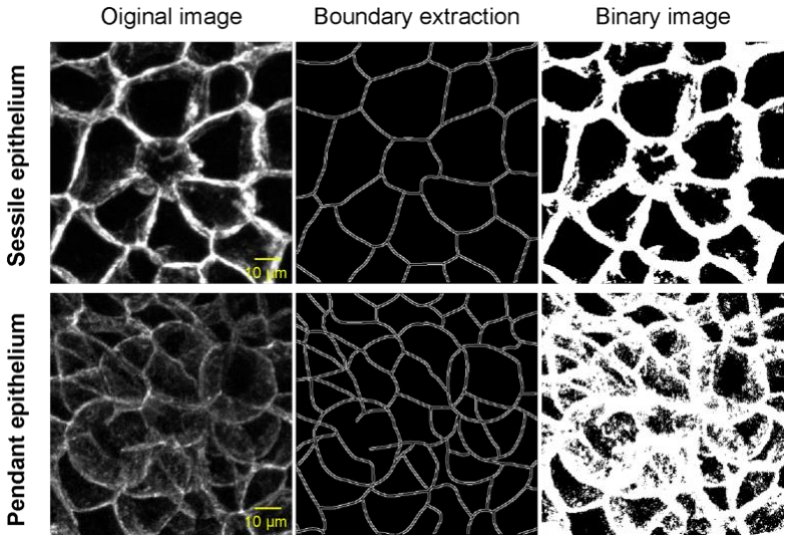

Figure. S6. Analysis of cell overlapping in the sessile and pendant epithelium. The boundary extraction and binary image generation were done using customized Matlab code. Within the identical area (2025 μm^2), the boundary length and fluorescence area in the sessile epithelium was about 390 μm and 794 μm^2, in contrast to 699 μm and 1284 μm^2 in the pendant epithelium. The significantly increased boundary length and fluorescence area indicated overlapping cells and disordered epithelial organization in the pendant epithelium.

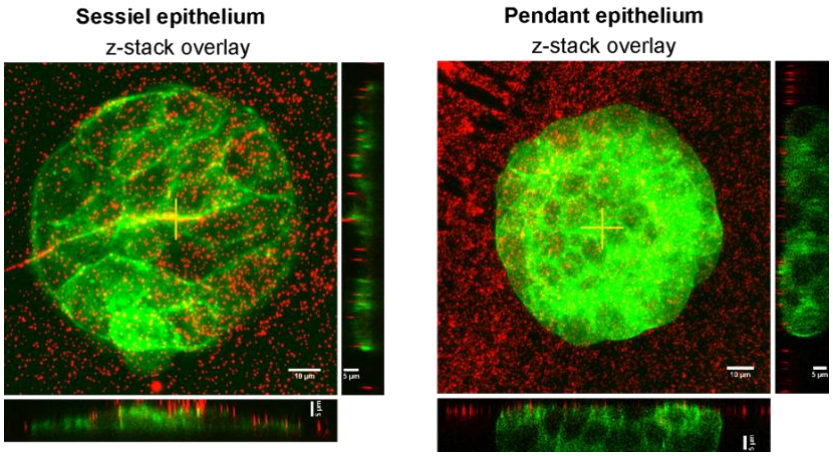

Figure S7. Presence of transepithelial forces in the sessile and pendant epithelia. MDCK cells were patterned into 100 um diameter circles onto soft (3 kPa) fibronectin-coated polyacrylamide substrates containing a monolayer of fluorescent nanobeads beneath the surface. Z-stack confocal images show the substrate was pushed down (as indicated by the monolayer of red microbeads) in the sessile epithelium (left), whereas no substrate deformation was seen in the tensile epithelium (right). The *yellows cross* denotes region of interest in the cross-sectional views.

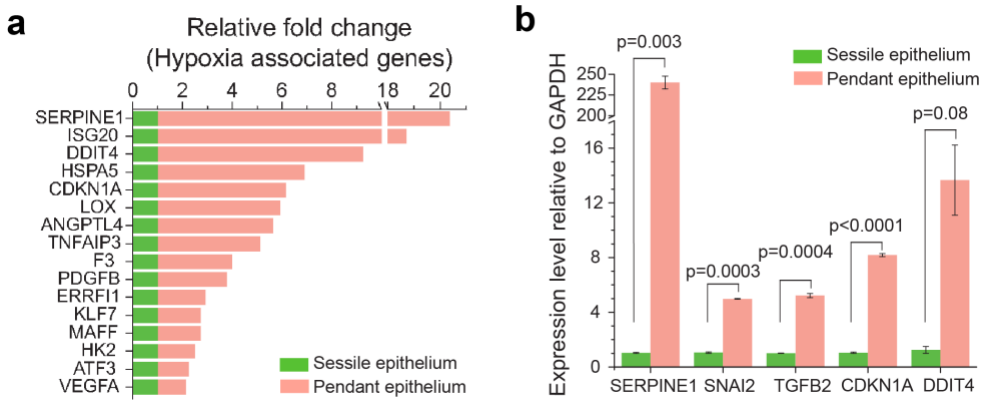

Figure S8. a), Upregulation of genes associated with hypoxia in the pendant epithelium. Hypoxia is a hallmark of tumor tissues, which could be caused by cell overlapping and multi-layered microdomain formation in the pendant epithelium. b), Expression levels of selected regulatory genes validated by RT-qPCR. SERPINE1 is related to bone morphogenetic protein (BMP) pathway, which was reported to regulate epithelial-mesenchymal transition (EMT). The upregulated *SNAI2* (a Snail-family factor) in the pendant epithelium is known to repress E-cadherin transcription and dampen cellular E-cadherin protein levels. *SNAI2* is also correlated with disruption of apicobasal polarity of epithelial cells. Data are shown as mean ± s.d.

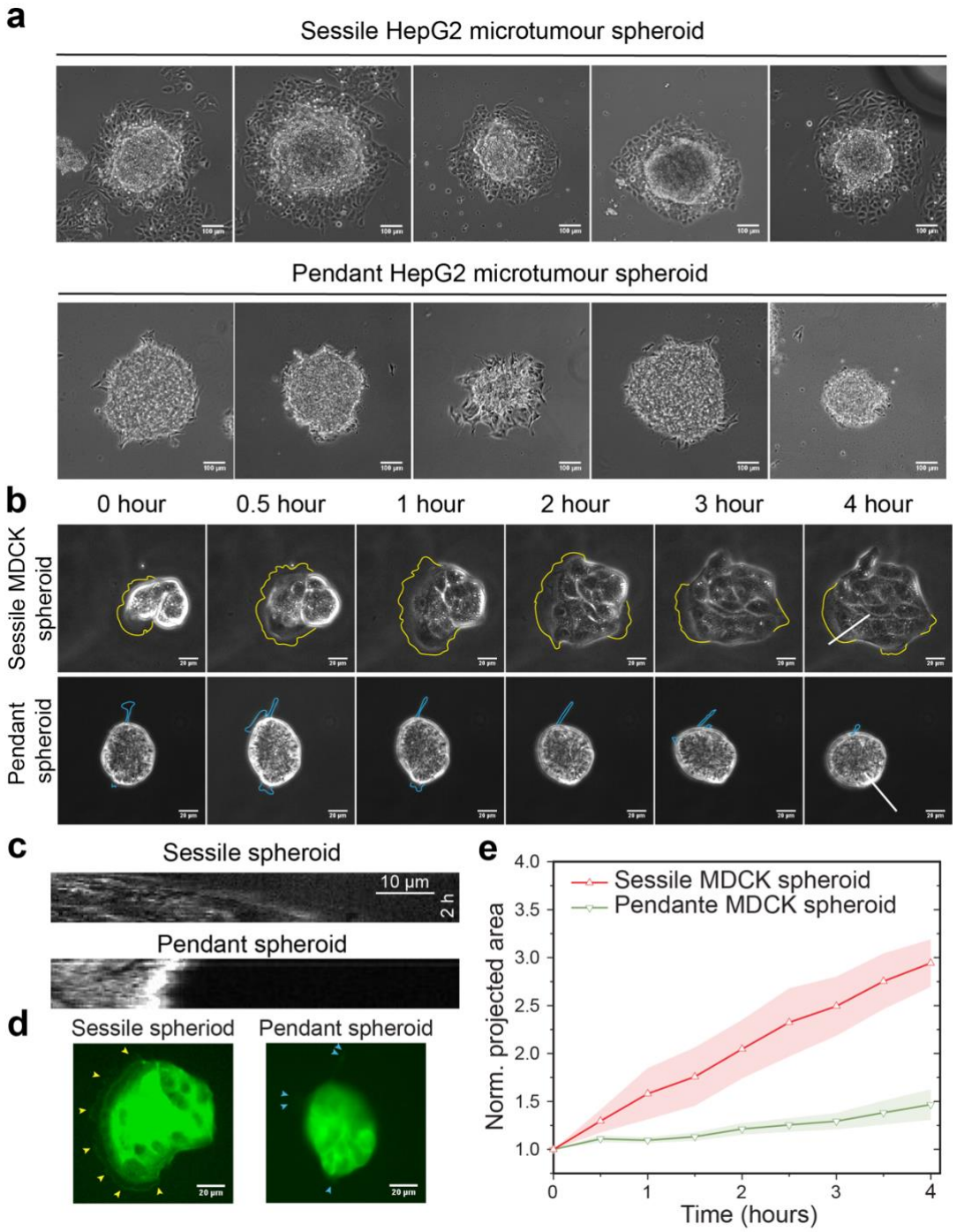

Figure S9. a) Differences in the lamination of HepG2 sessile and pendant microtumor spheroids after 19 hours. Sessile spheroids underwent robust lamination with a well-maintained epithelial morphology. By contrast, pendant spheroids were less prone to spreading and peripheral cells showed fibroblast-like morphology. b-e) Differences in the lamination of MDCK spheroids. b) Phase contrast images of sessile and pendant MDCK spheroids at different times. Sessile spheroids formed broad lamellipodium (yellow outline) during lamination while pendant spheroids formed and subsequently retracted filopodia (blue outline), allowing little to no spheroid lamination. c) Kymographs (obtained from regions indicated by white line in (b) show

the different speed of spheroid lamination. The sequential boundary of the sessile spheroid was extending robustly, whilst that of the pendant spheroid remained delaminated or even retracted. d) Confocal laser scanning microscopy further confirm the formation of broad lamellipodium (yellow arrowhead) in the spreading sessile spheroid and the formation of filopodia (blue arrowhead) in the pendant spheroid. Cells in the spheroids were tagged with GFP-actin. e) Graph shows sessile MDCK spheroids laminated at a faster rate than pendant spheroids. Within 4 hours, the projected spreading area of the sessile spheroid increased to 3 times of the original spheroids, whereas the pendant spheroid increased approximately 1.5 times. Data are from one experiment representative of six independent experiments (b-d) and are presented as mean ± seem (shaded areas) (e).

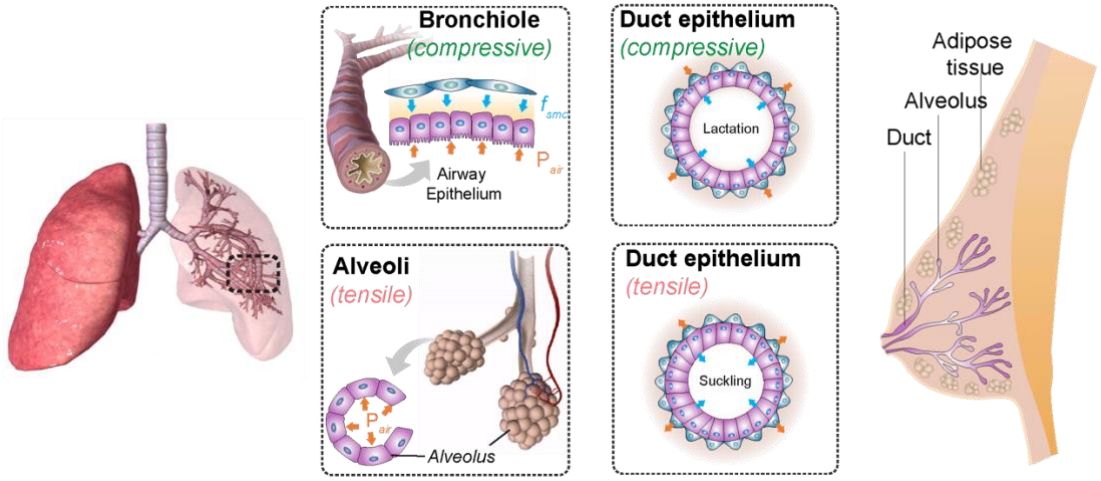

Figure S10. Transepithelially compressive and tensile stresses prevailing in human organs/ tissues. Schematic showing transepithelial compression can be found in the airway epithelium of constricting bronchiole and the lumen of lactating mammary glands (top), while transepithelial tension occurs in the expanding alveolus and mammary glands undergoing suckling (bottom).